A temporal multi-scale algorithm for efficient fluid modeling of a one-dimensional gas discharge

2014 Plasma Sources Sci. Technol. 23 065021

(http://iopscience.iop.org/0963-0252/23/6/065021)

IOP Publishing Plasma Sources Science and Technology

Plasma Sources Sci. Technol. **23** (2014) 065021 (12pp) doi:10.1088/0963-0252/23/6/065021

A temporal multi-scale algorithm for efficient fluid modeling of a one-dimensional gas discharge

B-R Gu[1], K-M Lin[1], M-H Hu[1], C-T Hung[1], J-S Wu[1,3] and Y-S Chen[2]

[1] Department of Mechanical Engineering, National Chiao Tung University, Hsinchu, Taiwan
[2] National Space Organization, National Applied Research Laboratories, Hsinchu, Taiwan

E-mail: chongsin@faculty.nctu.edu.tw

Received 31 December 2013, revised 6 July 2014
Accepted for publication 13 August 2014
Published 23 September 2014

Abstract

In this study, we present a temporal multi-scale algorithm (TMA) for efficient fluid modeling of a one-dimensional gas discharge with complex plasma chemistry. A helium dielectric barrier discharge driven by a power source with a frequency of 25 kHz is used as an example to demonstrate the superior capability of the TMA in accelerating fluid modeling simulations, while maintaining the same accuracy as compared to lengthy benchmarking fluid modeling using a single time-scale approach. The plasma chemistry considers 36 species and 121 reaction channels, which include some impurities such as nitrogen (25 ppm), oxygen (10 ppm) and water vapor (1 ppm), in addition to the helium itself. The results show that the runtime using the TMA can be dramatically reduced to 4% (25 times faster) with a relative difference of spatially averaged number densities generally less than 1% for all species between the TMA and the benchmarking cases when five initial cycles, five supplementary cycles and four repeated stages are used. Further reduction of the accuracy requirements to 44% for some specific species can lead to 92 times faster performance with the use of two initial cycles, two supplementary cycles and two repeated stages. The outlook for multi-dimensional fluid modeling considering a gas flow field is also described at the end of the paper.

Keywords: plasma fluid model (PFM), temporal multi-scale algorithm (TMA), helium, dielectric barrier discharge

(Some figures may appear in colour only in the online journal)

1. Introduction

Numerical modeling is a powerful tool for understanding low-temperature (or non-equilibrium) plasma (or a gas discharge) in detail, in addition to experimental observations. Among the various modeling tools, fluid modeling has played an important role in simulating various kinds of gas discharges at either intermediately low or atmospheric pressure, and in which the continuum assumption still holds [1, 2]. It solves the continuity, momentum and energy equations resulting from the velocity moments of the Boltzmann equation, for different kinds of species, including electrons, ions and neutrals. Large mass differences among these species lead to a very large disparity of time scales, ranging from 10^{-10} s for electrons 10^{-3} ~1 s or even longer for neutrals. No matter what kind of numerical scheme is used for solving these fluid modeling equations, one needs to resolve the time scale of electrons (~10^{-10} s) since they are a key species responsible for sustaining the gas discharge. In addition, one often needs to perform the simulation long enough to reach a true quasi-steady state for all species involved in the gas discharge, should the single time-step approach be employed. Unfortunately, the required runtime often becomes unacceptable because of the large time scales related to diffusion and convection processes associated with heavy neutral species. Thus, how to reduce the runtime required for reaching a true quasi-steady state for all species in a gas discharge becomes an important issue to be addressed for efficient and high-fidelity fluid modeling.

[3] Author to whom any correspondence should be addressed.

In general, there are three major approaches to reducing the computational time of fluid modeling. The first approach is to employ parallel computing for fluid modeling. Examples include the work of Lin *et al* [3, 4] who utilized MPI (message passing interface) for data communication among processors on a distributed-memory machine (e.g. a PC cluster). Depending upon the problem size (e.g. the number of grid points and species) and number of processors employed for parallel computing, they demonstrated that 1–2 orders of magnitude of time saving can be obtained using up to 100–200 processors. The second approach is to perform a sensitivity study to reduce the number of species and reactions to shorten the computational time. Gaens and Bogaerts [5] modeled an $Ar/N_2/O_2/H_2O$ plasma chemistry set with 84 species and 1880 reactions. They used for the criteria the relative contribution to the total generation/loss of a species. The results showed that the number of species and reactions can be reduced to 744 and 519 reactions, respectively, with a limited loss of accuracy. Liu *et al* [6] reduced He + H_2O plasma chemistry from 46 species and 577 reactions to 34 species and 89 reactions using a global model at atmospheric pressure. The third approach is to develop different multiple time-scale algorithms to couple these physical processes with wide ranging time scales. Examples include the works of Kushner [7], Lin *et al* [4], Sakiyama *et al* [8], and Sakiyama and Grave [9], in which the approach is the major focus of the current study.

Lin *et al* [4] proposed a temporal multi-scale method (TMSM), in addition to parallel computing, for modeling the two-dimensional atmospheric-pressure planar helium plasma jet (APPJ) in ambient air, in which both the fluid modeling and gas flow solvers are coupled. The TMSM considers only the source terms due to the chemical reactions by ignoring the transport terms (convection and diffusion) when integrating the continuity equations of heavy species (ions and neutrals) temporally at each electron time step. The transport terms are recovered only at integral numbers of electron time steps (5–50 or larger). They demonstrated that the total runtime reduction is only ∼50% at most for a fairly complex helium plasma chemistry (25 species and 101 reaction channels), in addition to parallel computing, because the marching time step is still based on the electron characteristic time scale for the whole time-integration process. Even with 300 processors it took nearly 1.5 months to reach 10 ms (∼250 cycles of 25 kHz driving power source), which is still not in a quasi-steady state for the APPJ under study. In summary, the TMSM only saves time when not solving the full continuity equations of heavy species for most of the time-integration process.

Later, Sakiyama *et al* [8] proposed a very complex plasma chemistry (53 species and 624 reaction channels) for modeling surface micro-discharges in humid air, in which two distinct layers, including the discharge region (charged and neutral species) and afterglow region (only neutral species), are assumed. The model is effectively a zero-dimensional approach (or 'global model'), in which the use of multiple time steps enables an efficient modeling of both the fast (reaction) and slow (diffusion) processes in the discharge layer and afterglow region, respectively, with a 'tight coupling' algorithm which will be explained later. They classified neutral species into short-lived (32 species) in the discharge layer and long-lived (21 species) in the afterglow region. A small time step was used for short-lived species as well as for long-lived and charged species for several cycles until a periodic steady state was reached. A much larger time step, e.g. 1 s, was used for long-lived species with the cycle-averaged rate constant from the simulation of short-lived species. The above two modules iterate between each other until convergence is found for the long-lived species. They presented the data for a time of more than 15 min (∼1000 s) using this approach with a total computational time of 100 h using a 4 dual-core processor at 2.1 GHz.

Recently, Sakiyama and Grave [9] presented a comparison of three coupling algorithms (tight coupling, one-way and weak coupling) between fast and slow processes for the global modeling of a similar problem (surface micro-discharge in humid air) as presented in Sakiyama *et al* [8]. The one-way coupling algorithm only solves the module of the short-lived, long-lived and charged species until they converge with a small time step, and then solves the module of the long-lived species until they converge with a much larger time step. The one-way coupling algorithm produces highly inaccurate results because of the lack of feedback from the long-lived species to the short-lived species, but is the fastest algorithm of the three. The weak coupling algorithm is a modified version of the tight coupling algorithm, in which the long-lived species are not updated during the calculations of the short-lived species. In this way, the set of ordinary differential equations may not become as 'stiff' as those of the tight coupling algorithm, which leads to faster convergence, as claimed by the authors. The results show that the weak coupling algorithm is ∼five times faster than the tight coupling algorithm with essentially the same accuracy (<15% difference for the major species).

Based on the above review, we understand that an efficient and accurate model for the multi-dimensional discharge problem with long-lived species involving drift, convection and diffusion processes requires further development. Thus, as a first step toward reaching this goal, we propose and validate a temporal multi-scale algorithm (TMA) for the general fluid modeling of a one-dimensional gas discharge with complex plasma chemistry. The investigation is justified by the inclusion of drift and diffusion in the 1D fluid model, in which the latter is often the slowest process in a typical discharge problem. Its future extension to two- and three-dimensional gas discharge problems considering thermal-fluid gas flow is also discussed briefly at the end of the paper.

The remainder of the paper is organized as follows. Section 2 describes the numerical methods proposed in this study, followed by the results of the validation presented in section 3. Finally, the major findings of the present study are summarized at the end of this paper.

2. Numerical methods

2.1. Fluid modeling equations

The fluid model we employ in the current study is basically the same as that presented by Lin *et al* [3] and is only

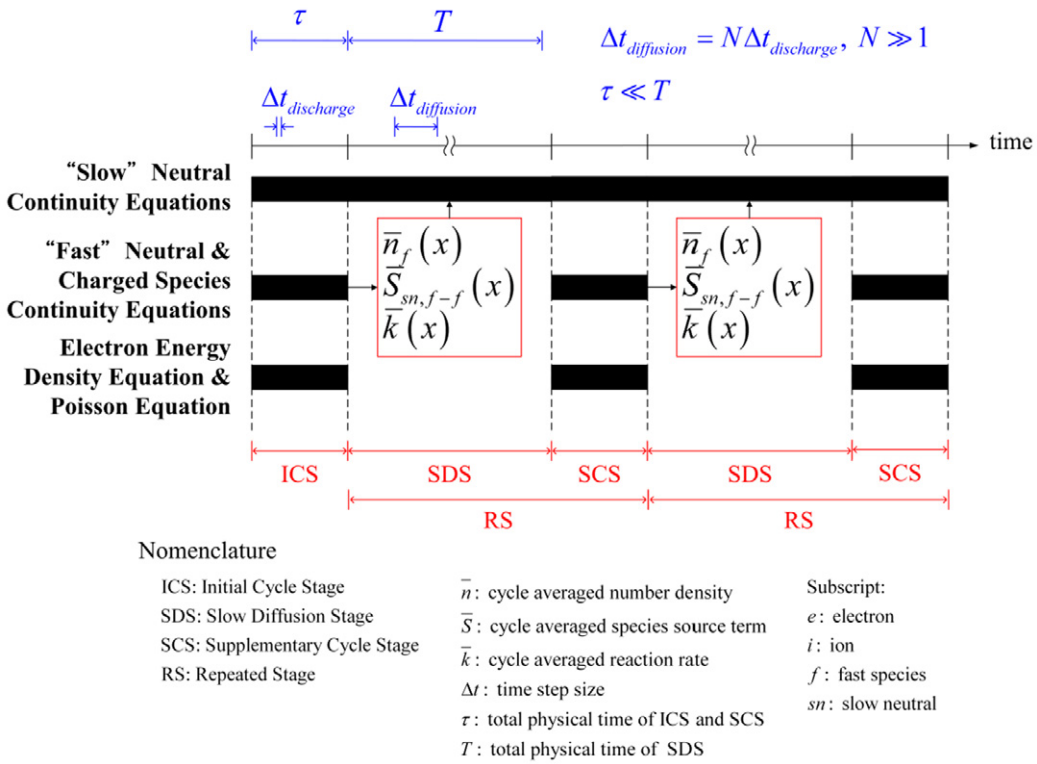

Figure 1. Schematic diagram of temporal multi-scale algorithm (TMA) for fluid modeling.

briefly described in the following for completeness. The fluid model includes the continuity equations for charged and neutral species, the momentum equations for charged and neutral species, the energy equation for electrons and Poisson's equation for electrostatic potential. No energy equations are solved for ions and various neutral species since they are assumed to be in thermal equilibrium with the background gas because of their heavy masses.

The general form of the continuity equation can be written as

$$\frac{\partial n_{e,i,N}}{\partial t} + \vec{\nabla} \cdot \vec{\Gamma}_{e,i,N} = S_{e,i,N} \tag{1}$$

where the subscripts e, i and N represent the electrons, ions and neutral species, respectively. The variables n, S and $\vec{\Gamma}$ stand for the number density, the source term resulting from the chemical reactions and the species flux vector, respectively. Based on the drift–diffusion approximation, the momentum equations are simplified as

$$\vec{\Gamma}_{e,i} = \text{sign}(q_{e,i})\mu_{e,i} n_{e,i} \vec{E} - D_{e,i} \vec{\nabla} n_{e,i} \tag{2}$$

$$\vec{\Gamma}_N = -D_N \vec{\nabla} n_N \tag{3}$$

where q, $\vec{E}$, $\vec{u}$, μ and D are the species charge, the electric field, the flow velocity vector, the mobility and the diffusivity, respectively.

Poisson's equation for electrostatic potential is written as

$$\nabla \cdot (\varepsilon \nabla \phi) = -\sum_{j=1}^{N_c} q_j n_j \tag{4}$$

where ε is the local permittivity which is a function of space (i.e. the material properties of the media), and N_c is the total number of charged species including electrons and ions. The corresponding electric field is then obtained through the relation $\vec{E} = -\nabla\phi$.

In addition, the electron energy density equation is expressed as

$$\frac{\partial (n_\varepsilon)}{\partial t} + \vec{\nabla} \cdot \vec{\Gamma}_{n_\varepsilon} = S_{n_\varepsilon} \tag{5}$$

where $n_\varepsilon \left(= \frac{3}{2} n_e k_B T_e\right)$ is the electron energy density, T_e is the electron temperature, and k_B is the Boltzmann constant. The electron energy density flux $\vec{\Gamma}_{n_\varepsilon} \left(= -\frac{5}{3}\mu_e \vec{E} n_\varepsilon - \frac{5}{3} D_e \vec{\nabla}(n_\varepsilon)\right)$ includes the drift and diffusion contributions similar to those in the continuity equations for the charged species. The source term S_{n_ε} stands for the summation of the energy losses due to elastic collisions, ionization, excitation, dissociation of electron-related chemical reactions, and the energy gain due to the Joule heating from the electric field.

The fluid modeling equations were discretized by the collocated cell-centered finite volume method in the spatial domain and the backward Euler's scheme in the temporal domain. The standard Scharfetter–Gummel scheme was employed for the fluxes of continuity equations and the electron energy density equation. More details of the implementation and validations can be found in Lin *et al* [3].

2.2. TMA for fluid modeling

Figure 1 shows the conceptual schematic diagram of the proposed TMA for fluid modeling without considering the gas flow effect. In what follows, we will use the dielectric barrier discharge (DBD) which is often driven by a power source

with a frequency of tens of kHz as an example to explain the procedure whenever necessary without losing the generality of the proposed TMA for other types of discharge with lower or higher driving frequencies. In the algorithm, we classify the neutral species into 'fast' and 'slow' neutral species. Note that 'fast' species represents both the 'fast' neutral species and the charged species hereafter. We can easily identify these by performing one-dimensional fluid modeling for a few cycles, in which the 'fast' neutral species respond to the driving time-dependent voltage similar to the charged species, and the 'slow' neutral species do not. Note that we have selected the 'fast' and 'slow' neutral species 'qualitatively', which, we have to admit, is the *ad hoc* element in the proposed TMA. More 'quantitative' methodology may be needed for a more precise selection of the 'fast' and 'slow' neutral species in the future. The basic idea of the TMA is to integrate those species temporally that respond quickly and slowly to the driving voltage with a small (electron-limited) and large (diffusion-limited) time step, respectively, in which temporal synchronization is approximately maintained between the 'slow' neutral species and 'fast' species. To maintain approximate synchronization among all species, we have involved all the species in the time-integration process with the small time step and only involved 'slow' neutral species in the time integration with the large time step. The mechanism to fulfill this goal is to 'freeze' the number densities of the 'fast' species and 'pump in' exactly the time-dependent source terms due to the chemical reactions for producing and destroying the 'slow' neutral species during the time integration of the 'slow' neutral species with a very large time step. In this way, we can take advantage of the very large time step used for the 'slow' neutral species to reach the steady-state solution much more quickly, which is otherwise practically impossible with the small time step used for the 'fast' species.

Before describing the details of the simulation procedures of the TMA, two important parameters that will be used for the time-integration process of 'slow' species are defined, including the cycle-averaged number densities of the 'fast' species (equation (6)) and the time-dependent reaction source terms of the 'slow' neutral species due to the chemical reactions (equation (7)). Note the latter may involve the reactions with reactants of 'fast' species with 'fast' species, 'slow' neutral species with 'slow' neutral species and 'slow' neutral species with 'fast' species, which are defined in equation (8) through equation (10) respectively:

$$\bar{n}_{fi}(x) = \frac{1}{T}\int_0^T n_{fi}(t,x)\,\mathrm{d}t \tag{6}$$

$$S_{snj}(t,x) = \bar{S}_{snj,f-f}(x) + S_{snj,sn-sn}(t,x) + S_{snj,sn-f}(t,x) \tag{7}$$

$$\bar{S}_{snj,f-f}(x) = \sum_{i=1}^{N_{snj,f-f}} \left[\frac{1}{T}\int_0^T k_{ji}(t,x)\, n_{fl}(t,x)\, n_{fm}(t,x)\,\mathrm{d}t\right] \tag{8}$$

$$S_{snj,sn-sn}(t,x) = \sum_{i=1}^{N_{snj,sn-sn}} \bar{k}_{ji}(x) n_{snl}(t,x)\, n_{snm}(t,x) \tag{9}$$

$$S_{snj,sn-f}(t,x) = \sum_{i=1}^{N_{snj,sn-f}} \bar{k}_{ji}(x) n_{snl}(t,x)\, \bar{n}_{fm}(x). \tag{10}$$

The subscripts f and sn refer to the 'fast' species and 'slow' neutral species respectively. In addition, n, S and T stand for the number density, reaction source term and period of driving power source, respectively. The bars of $\bar{n}$, $\bar{k}$ and $\bar{S}$ stand for the cycle-averaged value of each variable, respectively. Note k_{ji} refers to the rate constant of the ith reaction channel related to the 'slow' species j. The terms $N_{snj,f-f}$, $N_{snj,sn-sn}$ and $N_{snj,sn-f}$ represent the numbers of reaction channels that involve the 'fast' species only, 'slow' neutral species only and both 'slow' neutral species and 'fast' species in the reactants, respectively, which generate or destroy the 'slow' neutral species j. The terms $\bar{S}_{snj,f-f}$, $S_{snj,sn-sn}$ and $S_{snj,sn-f}$ represent the source terms of the 'slow' neutral species j, resulting from these three types of reaction channels. The subscripts l and m denote the reactants participating in the specific reaction channel i.

The major simulation procedures based on figure 1 are summarized as follows.

1. *Initial cycle stage (ICS).* The simulation starts with some initial conditions and runs for several initial cycles until it reaches a periodic steady state. In this stage, all charged and neutral species are integrated with a small marching time step (i.e. $\Delta t_{\mathrm{discharge}}$) constrained by the electron, during which two categories of cycle-averaged data are calculated and stored: (1) the number densities of charged and 'fast' neutral species, as shown in equation (6), and (2) the reaction source terms of 'slow' neutral species purely due to 'fast' species, as shown in equation (8).
2. *Slow diffusion stage (SDS).* In this stage, only the continuity equations for 'slow' neutral species are solved using the cycle-averaged data obtained from the ICS with a diffusion-limited (large) time step (i.e. $\Delta t_{\mathrm{diffusion}} = N\Delta t_{\mathrm{discharge}}$, where $N \gg 1$) until either a preset physical time (e.g. tens of thousands of cycles or more) or convergence criteria for a steady state are reached. The source terms of the continuity equations of 'slow' neutral species are calculated following equation (7). The size of the SDS can be approximately determined by the largest characteristic diffusive time scale among the 'slow' neutral species estimated by $\tau_{\mathrm{diffusion}} \sim \frac{l^2}{D}$, where $\tau_{\mathrm{diffusion}}$ is the characteristic diffusive time scale,l is the characteristic length (e.g. gap distance in the current study) and D is the diffusion coefficient.
3. *Supplementary cycle stage (SCS).* Similar to the ICS, the fluid modeling is performed involving all species using the number densities of 'slow' neutrals resulting from the SDS as the initial conditions until either a preset physical time (e.g. few cycles) is reached or a quasi-steady state emerges. As mentioned earlier, the inclusion of the 'slow' neutral species in this stage is beneficial since it will synchronize temporally among all species; also, its computational overhead is relatively small since the continuity equations for the 'slow' neutral species are typical parabolic-type partial differential equations (i.e. time-dependent diffusion–reaction type equations) with small (non-stiff) source terms because of the smaller time step used for time integration in the SCS. Of course, its computational cost increases with increasing number of the 'slow' neutral species.

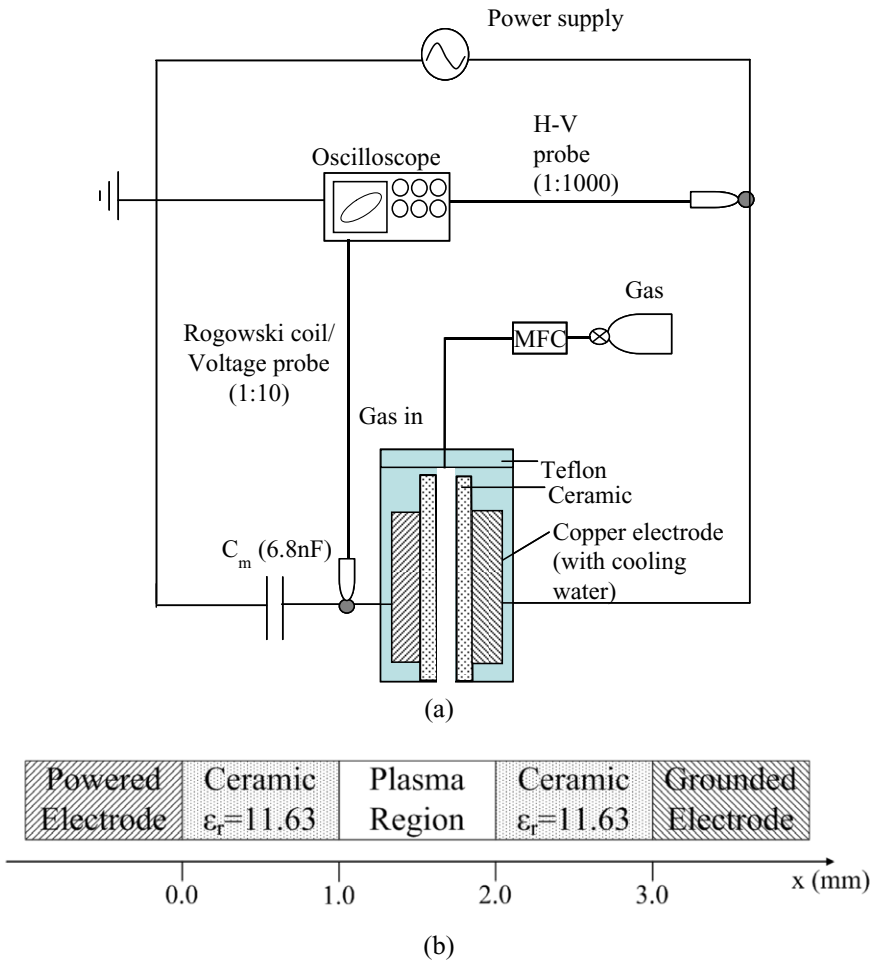

Figure 2. (*a*) Sketch of the planar helium AP-DBD system [10] and (*b*) simplified diagram for 1D helium DBD.

4. *Repeated stage (RS).* Return to step 2, repeat the process until the preset criteria are satisfied and then output the required data and stop.

Note that the above procedures can be easily adapted, should the gas flow be considered for a multi-dimensional discharge problem, which will be described briefly in the conclusion section.

3. Results and discussion

Figure 2 illustrates the schematic diagram of the planar atmospheric-pressure dielectric barrier discharge (AP-DBD) we used for the purpose of demonstrating the proposed TMA for one-dimensional fluid modeling. It consists of two electrodes (power and ground), each covered with a dielectric layer (with a relative permittivity of 11.63) of 1 mm in thickness and a plasma region with a gap distance of 1 mm. The geometrical configuration is the same as that presented in the experimental work of Chiang *et al* [10]. In our recent experiments, commercially available helium (99.99% purity) was used as the discharge gas that flows through the parallel plate. We carefully measured the composition of several bottles using gas chromatography (GC) and found that the average levels of impurities are 25 ppm and 10 ppm for nitrogen and oxygen, respectively. The water vapor level, which we estimated to be 1 ppm for the modeling purpose, is too low to be measured accurately using GC. Thus, we have included impurities such as oxygen, nitrogen and water vapor at these levels in our fluid model. Table 1 summarizes the major simulation conditions used for one-dimensional fluid modeling, in which a sinusoidal voltage waveform ($V_{\mathrm{p-p}} = 6$ kV and frequency $= 25$ kHz) was used as the power source. In addition, 50 non-uniform computational cells were used for the simulation after a careful grid convergence test and the simulation time step size ($\Delta t_{\mathrm{discharge}}$) was kept as 5×10^{-10} s throughout the study, unless otherwise specified. It took approximately 40 h of runtime on a PC (Intel Woodcrest, 3.0 GHz and 4 GB RAM) to reach a physical time of ~0.04 s at which time it was considered to be in a quasi-steady state for this specific problem. In addition, when TMA is used, the time step size ($\Delta t_{\mathrm{diffusion}}$) during the SDS is set as 4×10^{-7} s (~800 times larger than $\Delta t_{\mathrm{discharge}}$) for marching those 'slow' neutral species in time, which runs for 25 000 time steps, or 0.01 s (physical time) for each SDS. Note the time step size can be much larger without losing solution accuracy in the current test problem. Both the benchmarking and all the TMA cases use identical initial number densities, unless otherwise specified.

In the plasma chemistry, we considered 36 species (e, He^+, He_2^+, O^+, O_2^+, O^-, O_2^-, N^+, N_2^+, N_4^+, OH^+, H_2O^+,

Table 1. Simulation conditions of helium DBD with impurities including oxygen, nitrogen and water vapor.

Simulation conditions	
Pressure (Pa)	760 Torr
Temperature (K)	400 K
Composition of background gas	
He (ppm)	99.9964%
N_2	25 ppm
O_2	10 ppm
H_2O	1 ppm
Power source	
V_{p-p}	6.0 kV
Frequency	25 kHz
Waveform	Sinusoidal
Plasma chemistry	
Number of species	36
Number of reactions	121

Table 2. Summary of modeled species of helium DBD with impurities of oxygen, nitrogen and water vapor. The 'fast species' represents the electron, ions and the 'fast' neutral species.

		Species
Fast species	Electron	e
	Ions	He^+, He_2^+, O^+, O_2^+, O^-, O_2^-, N^+, N_2^+, N_4^+, OH^+, H_2O^+, H_3O^+, $H_5O_2^+$, $H_7O_3^+$, $H_9O_4^+$
	Fast neutral	He_m^*, He_{ex}^*, He_2^*, $O(^1D)$, $N_2(B\,^3\Pi_g)$, $N_2(C\,^3\Pi_u)$, $OH(A)$
Slow neutral		O, $O(^1S)$, $O_2(a\,^1\Delta_g)$, O_3, NO, $N(^2D)$, $N(^4S)$, $N_2(A\,^3\Sigma_u^+)$, $N_2(a'\,^1\Sigma_u^-)$, H, H_2, OH, H_2O_2

H_3O^+, $H_5O_2^+$, $H_7O_3^+$, $H_9O_4^+$, He_m^*, He_{ex}^*, He_2^*, O_3, O, $O(^1D)$, $O(^1S)$, $O_2(a\,^1\Delta_g)$, NO, $N_2(A\,^3\Sigma_u^+)$, $N_2(B\,^3\Pi_g)$, $N_2(a'\,^1\Sigma_u^-)$, $N_2(C\,^3\Pi_u)$, $N(^2D)$, $N(^4S)$, H, H_2, OH, $OH(A)$, H_2O_2) and 121 reaction channels, as listed in tables 2 and 3 respectively. In table 2, we also classify the neutrals into 'fast' and 'slow' neutrals based on a preliminary run of the fluid code for several cycles, as described earlier. It turns out that there are 7 'fast' neutral species and 13 'slow' neutral species, the classification of which strongly depends upon the chemical kinetics and has no correlation with their molecular weights. Reaction channels (R0)–(R26) consider the chemistry for a pure helium discharge. Reaction channels (R27)–(R42) describe the chemistry of oxygen and its interaction with helium, (R43)–(R63) model the chemistry of N_2 and its interaction with helium, (R64)–(R100) consider the interaction between O_2 and N_2, and (R101)–(R120) define the interaction between helium and water vapor.

The transport coefficients and the rate constants related to the electrons are calculated by solving the Boltzmann equation using BOLSIG$^+$ [11]. Note that these coefficients are predicted and stored in a lookup table as a function of electron temperature. The mobility data of the ions are taken from the literature [12–17], and the corresponding diffusivity data are calculated using the Einstein relation. As for the diffusion coefficients of neutral species, such as He_m^*, He_{ex}^*, He_2^*, O_3, O, N and OH, they are found from the literature wherever available [12, 14, 18]. Those of NO, H_2 and H_2O_2 are calculated from the Chapman–Enskog equation for binary diffusion [19], in which the required parameters for calculating the diffusivity can be found from Poling *et al* [20]. The diffusivities of excited neutral species are assumed to be equal to those of the corresponding ground-state neutral species since these properties are rarely found in the literature.

Figure 3 shows the comparison of temporal variations of the spatially averaged number densities of all the 'fast' species, including the charged and the 'fast' neutral species, in the last ac cycle between the benchmarking and TMA cases (five initial cycles (ICs), five supplementary cycles (SCs) and four repetitions (RSs)). The reason for choosing five SCs when four RSs are fixed for the typical simulation is mainly because with five SCs we can guarantee that the relative differences of all species with benchmarking are less than 1%. The results show that the two sets of data are essentially the same at all times in the last cycle, which proves that the proposed TMA does reproduce the correct temporal evolution of the densities of all the 'fast' species for the 1D fluid model. In addition, the concentrations of some of the 'fast' neutral species such as He_m^* and He_2^* are in the order of $10^{18}\,m^{-3}$, which is much higher than those of the charged species, and agree with some previous simulations for helium DBD (e.g. [21, 22]).

Figure 4 shows the corresponding temporal variations of the spatially averaged number densities of the 'slow' neutral species using the TMA with the same simulation conditions (five ICs, five SCs and four RSs) as presented in figure 3. To test the sensitivity of the initial conditions on the transient time required for the 'slowest' neutral species among all 'slow' species in reaching a steady state in the TMA, we have applied various initial conditions: (1) distributed initial densities (figure 4(*a*)), (2) low initial densities (figure 4(*b*)), and (3) high initial densities (figure 4(*c*)). In figure 4(*c*), the densities of several 'slow' neutral species (e.g. $N(^4S)$, OH and H_2O_2) decrease dramatically in the first SDS (0.0002–0.01 s) mainly because the cycle-averaged chemical sink terms for these 'slow' neutral species obtained in the ICS become too negative, which leads to the rapid consumption of these species in the first SDS. All data show that they converge to almost exactly the same solution after ~0.02 s, which demonstrates the robustness of the proposed TMA. In the current test problem, the 'slowest' neutral species is $O_2\left(a\,^1\Delta_g\right)$ and its characteristic diffusive time scale is estimated to be 0.018 s, based on $\tau_{diffusion} \sim \frac{l^2}{D}$, where $\tau_{diffusion}$ is the characteristic diffusive time scale, l (= 1 mm) is the characteristic length and D (= $5.51 \times 10^{-5}\,m^2\,s^{-1}$) is the diffusion coefficient. The results show that the transient times for $O_2\left(a\,^1\Delta_g\right)$ are approximately of the same order as the estimated characteristic diffusive time scale, except that the estimated initial density of $O_2\left(a\,^1\Delta_g\right)$ in figure 4(*a*) is 'accidentally' too close to the steady-state solution.

Figure 4 also shows that atomic oxygen ($\sim 3.4 \times 10^{18}\,m^{-3}$) and hydrogen peroxide ($\sim 8.4 \times 10^{14}\,m^{-3}$) are the most and least abundant species, respectively, among these 'slow' neutral species. The density of atomic oxygen is one order

Table 3. Summary of helium plasma chemistry considering impurities (nitrogen, oxygen and water vapor).

No	Reaction channels	Rate constant or cross section	Threshold (eV)	Ref.
(R00)	$e + He \rightarrow e + He$	BOLSIG+	0	[24]
(R01)	$e + He \rightarrow e + He_m^*$	BOLSIG+	19.82	[24]
(R02)	$e + He \rightarrow e + He_m^*$	BOLSIG+	20.61	[24]
(R03)	$e + He \rightarrow e + He_{ex}^*$	BOLSIG+	20.96	[24]
(R04)	$e + He \rightarrow e + He_{ex}^*$	BOLSIG+	21.21	[24]
(R05)	$e + He \rightarrow e + He_{ex}^*$	BOLSIG+	22.97	[24]
(R06)	$e + He \rightarrow e + He_{ex}^*$	BOLSIG+	23.7	[24]
(R07)	$e + He \rightarrow e + He_{ex}^*$	BOLSIG+	24.02	[24]
(R08)	$e + He \rightarrow 2e + He^+$	BOLSIG+	24.58	[24]
(R09)	$e + He_m^* \rightarrow 2e + He^+$	BOLSIG+	4.78	[24]
(R10)	$e + He_m^* \rightarrow e + He$	$2.9 \times 10^{-15}\ m^3\ s^{-1}$	−19.8	[24]
(R11)	$e + He_2^* \rightarrow e + 2He$	$3.8 \times 10^{-15}\ m^3\ s^{-1}$	−17.9	[24]
(R12)	$He^+ + 2e \rightarrow e + He_m^*$	$6 \times 10^{-32}\ m^6\ s^{-1}$	−4.78	[24]
(R13)	$He_2^+ + 2e \rightarrow He_m^* + He + e$	$2.8 \times 10^{-32}\ m^6\ s^{-1}$	0	[24]
(R14)	$He_2^+ + e + He \rightarrow He_m^* + 2He$	$3.5 \times 10^{-39}\ m^6\ s^{-1}$	0	[24]
(R15)	$He_2^+ + 2e \rightarrow He_2^* + e$	$1.2 \times 10^{-33}\ m^6\ s^{-1}$	0	[24]
(R16)	$He_2^+ + e + He \rightarrow He_2^* + He$	$1.5 \times 10^{-39}\ m^6\ s^{-1}$	0	[24]
(R17)	$He_{ex}^* + He \rightarrow He_2^+ + e$	$1.5 \times 10^{-17}\ m^3\ s^{-1}$	0	[24]
(R18)	$He_m^* + He_m^* \rightarrow He_2^+ + e$	$2.03 \times 10^{-15}\ m^3\ s^{-1}$	−18.2	[24]
(R19)	$He_m^* + He_m^* \rightarrow He^+ + He + e$	$8.7 \times 10^{-16}\ m^3\ s^{-1}$	−15.8	[24]
(R20)	$He^+ + 2He \rightarrow He_2^+ + He$	$6.5 \times 10^{-44}\ m^6\ s^{-1}$	0	[24]
(R21)	$He_m^* + 2He \rightarrow He_2^* + He$	$1.9 \times 10^{-46}\ m^6\ s^{-1}$	0	[24]
(R22)	$He_m^* + He_2^* \rightarrow He^+ + 2He + e$	$5 \times 10^{-16}\ m^3\ s^{-1}$	−13.5	[24]
(R23)	$He_m^* + He_2^* \rightarrow He_2^+ + He + e$	$2 \times 10^{-15}\ m^3\ s^{-1}$	−15.9	[24]
(R24)	$He_2^* + He_2^* \rightarrow He^+ + 3He + e$	$3 \times 10^{-16}\ m^3\ s^{-1}$	−11.3	[24]
(R25)	$He_2^* + He_2^* \rightarrow He_2^+ + 2He + e$	$1.2 \times 10^{-15}\ m^3\ s^{-1}$	−13.7	[24]
(R26)	$He_2^* + He \rightarrow 3He$	$4.9 \times 10^{-22}\ m^3\ s^{-1}$	0	[24]
(R27)	$e + O_2 \rightarrow e + O_2$	BOLSIG+	0	[25]
(R28)	$e + O_2 \rightarrow 2e + O_2^+$	BOLSIG+	12.06	[25]
(R29)	$e + 2O_2 \rightarrow O_2^- + O_2$	BOLSIG+	0	[25]
(R30)	$O_3 + O \rightarrow 2O_2$	$8.3 \times 10^{-21}\ m^3\ s^{-1}$	0	[25]
(R31)	$e + O_2^+ \rightarrow 2O$	$4.8 \times 10^{-13}\ m^3\ s^{-1}$	0	[25]
(R32)	$O^+ + O_2 \rightarrow O_2^+ + O$	$2.0 \times 10^{-17}\ m^3\ s^{-1}$	0	[25]
(R33)	$He_m^* + O_2 \rightarrow e + O_2^+ + He$	$2.4 \times 10^{-16}\ m^3\ s^{-1}$	0	[25]
(R34)	$He_m^* + O \rightarrow e + O^+ + He$	$4.3 \times 10^{-16}\ m^3\ s^{-1}$	0	[25]
(R35)	$2O + He \rightarrow He + O_2$	$1.04 \times 10^{-45}\ m^6\ s^{-1}$	0	[25]
(R36)	$O + He + O_2 \rightarrow O_3 + He$	$6.27 \times 10^{-46}\ m^6\ s^{-1}$	0	[25]
(R37)	$O_3 + He \rightarrow O + He + O_2$	$2.28 \times 10^{-32}\ m^3\ s^{-1}$	0	[25]
(R38)	$e + O_2 \rightarrow O + O^-$	BOLSIG+	0	[26]
(R39)	$e + O_2 \rightarrow e + O_2(a)$	BOLSIG+	0.977	[26]
(R40)	$e + O_2 \rightarrow e + 2O$	BOLSIG+	6.0	[26]
(R41)	$e + O_2 \rightarrow e + O + O(^1D)$	BOLSIG+	8.4	[26]
(R42)	$e + O_2 \rightarrow e + O + O(^1S)$	BOLSIG+	10.0	[26]
(R43)	$He_m^* + N_2 \rightarrow e + N_2^+ + He$	$7.0 \times 10^{-17}\ m^3\ s^{-1}$	0	[12]
(R44)	$He_2^* + N_2 \rightarrow e + N_2^+ + 2He$	$7.0 \times 10^{-17}\ m^3\ s^{-1}$	0	[12]
(R45)	$He^+ + N_2 \rightarrow N_2^+ + He$	$5.0 \times 10^{-16}\ m^3\ s^{-1}$	0	[12]
(R46)	$He^+ + N_2 \rightarrow N^+ + N + He$	$7.0 \times 10^{-16}\ m^3\ s^{-1}$	0	[12]
(R47)	$He_2^+ + N_2 \rightarrow N_2^+ + 2He$	$5.0 \times 10^{-16}\ m^3\ s^{-1}$	0	[12]
(R48)	$He_2^+ + N_2 \rightarrow N^+ + N + 2He$	$7.0 \times 10^{-16}\ m^3\ s^{-1}$	0	[12]
(R49)[a]	$2e + N_2^+ \rightarrow e + N_2$	$5.651 \times 10^{-39} T_e^{-0.8}\ m^6\ s^{-1}$	0	[12]
(R50)[a]	$e + N_2^+ \rightarrow 2N$	$2.540 \times 10^{-12} T_e^{-0.5}\ m^3\ s^{-1}$	0	[12]
(R51)[a]	$e + N_2 \rightarrow e + 2N$	$1.959 \times 10^{-12} T_e^{-0.7} \exp\left(-\frac{1.132\times10^5}{T_e}\right)\ m^3\ s^{-1}$	9.757	[12]
(R52)[a]	$e + N \rightarrow 2e + N^+$	$8.401 \times 10^{-11} \exp\left(-\frac{1.682\times10^5}{T_e}\right)\ m^3\ s^{-1}$	14.5	[12]
(R53)	$e + N_2 \rightarrow e + N_2$	BOLSIG+	0.0	[26]
(R54)	$e + N_2 \rightarrow 2e + N_2^+$	BOLSIG+	15.581	[26]
(R55)	$e + N_2 \rightarrow e + N_2\ (A\,^3\Sigma_u^+)$	BOLSIG+	6.169	[26]
(R56)	$e + N_2 \rightarrow e + N_2\ (B\,^3\Pi_g)$	BOLSIG+	7.353	[26]
(R57)	$e + N_2 \rightarrow e + N_2\ (C\,^3\Pi_u)$	BOLSIG+	11.032	[26]
(R58)	$e + N_2 \rightarrow e + N_2\ (a'\,^1\Sigma_u^-)$	BOLSIG+	8.399	[26]
(R59)[a]	$e + N_4^+ \rightarrow 2N_2$	$2.0 \times 10^{-12} \left(\frac{T_g}{T_e}\right)^{0.5}\ m^3\ s^{-1}$	0.0	[27]
(R60)	$N_2^+ + 2N_2 \rightarrow N_4^+ + N_2$	$1.9 \times 10^{-41}\ m^6\ s^{-1}$	0.0	[27]
(R61)	$N_2^+ + He + N_2 \rightarrow N_4^+ + He$	$1.9 \times 10^{-41}\ m^6\ s^{-1}$	0.0	[27]

Table 3. (Continued.)

No	Reaction channels	Rate constant or cross section	Threshold (eV)	Ref.
(R62)	$N_4^+ + N_2 \rightarrow N_2^+ + 2N_2$	2.5×10^{-21} m^3 s^{-1}	0.0	[27]
(R63)	$N_4^+ + He \rightarrow N_2^+ + He + N_2$	2.5×10^{-21} m^3 s^{-1}	0.0	[27]
(R64)	$N_2(A\,^3\Sigma_u^+) + N_2(a'\,^1\Sigma_u^-) \rightarrow e + N_4^+$	5.0×10^{-17} m^3 s^{-1}	0.0	[28]
(R65)	$2N_2(a'\,^1\Sigma_u^-) \rightarrow e + N_4^+$	2.0×10^{-16} m^3 s^{-1}	0.0	[28]
(R66)	$e + N_2^+ \rightarrow N(^2D) + N$	3.7×10^{-13} m^3 s^{-1}	0.0	[26]
(R67)	$e + O_2^+ \rightarrow O + O(^1D)$	2.1×10^{-13} m^3 s^{-1}	0.0	[26]
(R68)	$O_2^+ + O_2^- \rightarrow 2O_2$	7.8×10^{-12} m^3 s^{-1}	0.0	[26]
(R69)	$O^- + N_2^+ \rightarrow O + N_2$	7.8×10^{-12} m^3 s^{-1}	0.0	[26]
(R70)	$O_2^+ + O^- \rightarrow O + O_2$	7.5×10^{-12} m^3 s^{-1}	0.0	[26]
(R71)	$O_2^- + O_2(a) \rightarrow e + 2O_2$	2.0×10^{-16} m^3 s^{-1}	0.0	[26]
(R72)	$O_2^- + N_2(A\,^3\Sigma_u^+) \rightarrow e + O_2 + N_2$	2.1×10^{-15} m^3 s^{-1}	0.0	[26]
(R73)	$O_2^- + N_2(B\,^3\Pi_g) \rightarrow e + O_2 + N_2$	2.5×10^{-15} m^3 s^{-1}	0.0	[28]
(R74)	$O^- + O_2(a) \rightarrow e + O_3$	3.0×10^{-16} m^3 s^{-1}	0.0	[28]
(R75)	$O^- + N_2(A\,^3\Sigma_u^+) \rightarrow e + O + N_2$	2.2×10^{-15} m^3 s^{-1}	0.0	[26]
(R76)	$O^- + N_2(B\,^3\Pi_g) \rightarrow e + O + N_2$	1.9×10^{-15} m^3 s^{-1}	0.0	[28]
(R77)	$O_2^- + O \rightarrow e + O_3$	1.5×10^{-16} m^3 s^{-1}	0.0	[26]
(R78)	$O^- + O \rightarrow e + O_2$	5.0×10^{-16} m^3 s^{-1}	0.0	[26]
(R79)	$O^- + N \rightarrow e + NO$	2.6×10^{-16} m^3 s^{-1}	0.0	[26]
(R80)	$O^- + O_2 \rightarrow e + O_3$	5.0×10^{-21} m^3 s^{-1}	0.0	[28]
(R81)	$O + N + N_2 \rightarrow NO + N_2$	$1.76 \times 10^{-43} \times T_g^{-0.5}$ m^6 s^{-1}	0.0	[28]
(R82)	$O + O_2 + N_2 \rightarrow O_3 + N_2$	5.6×10^{-46} m^6 s^{-1}	0.0	[26]
(R83)	$N_2(A\,^3\Sigma_u^+) + O_2 \rightarrow 2O + N_2$	1.7×10^{-18} m^3 s^{-1}	0.0	[26]
(R84)	$N_2(A\,^3\Sigma_u^+) + O_2 \rightarrow O_2(a) + N_2$	7.5×10^{-19} m^3 s^{-1}	0.0	[26]
(R85)	$O + N_2(A\,^3\Sigma_u^+) \rightarrow NO + N(^2D)$	7.0×10^{-19} m^3 s^{-1}	0.0	[26]
(R86)	$O + N_2(A\,^3\Sigma_u^+) \rightarrow O(^1S) + N_2$	2.3×10^{-17} m^3 s^{-1}	0.0	[26]
(R87)	$N_2(B\,^3\Pi_g) + N_2 \rightarrow N_2(A\,^3\Sigma_u^+) + N_2$	3.0×10^{-17} m^3 s^{-1}	0.0	[26]
(R88)	$N_2(B\,^3\Pi_g) + O_2 \rightarrow 2O + N_2$	1.1×10^{-16} m^3 s^{-1}	0.0	[26]
(R89)	$N_2(a'\,^1\Sigma_u^-) + O_2 \rightarrow 2O + N_2$	2.8×10^{-17} m^3 s^{-1}	0.0	[26]
(R90)	$NO + N_2(a'\,^1\Sigma_u^-) \rightarrow O + N + N_2$	3.6×10^{-16} m^3 s^{-1}	0.0	[26]
(R91)	$N_2(C\,^3\Pi_u) + N_2 \rightarrow N_2(a'\,^1\Sigma_u^-) + N_2$	1.0×10^{-17} m^3 s^{-1}	0.0	[26]
(R92)	$N_2(C\,^3\Pi_u) + O_2 \rightarrow O + O(^1S) + N_2$	3.0×10^{-16} m^3 s^{-1}	0.0	[26]
(R93)	$N(^2D) + O_2 \rightarrow O + NO$	$1.5 \times 10^{-18} \times (T_g/300)^{0.5}$ m^3 s^{-1}	0.0	[28]
(R94)	$N(^2D) + O_2 \rightarrow O(^1D) + NO$	6.0×10^{-18} m^3 s^{-1}	0.0	[26]
(R95)	$O(^1D) + O_2 \rightarrow O + O_2(a)$	3.4×10^{-17} m^3 s^{-1}	0.0	[26]
(R96)	$O(^1D) + O_2 \rightarrow O + O_2$	$6.4 \times 10^{-18} \times \exp(67/T_g)$ m^3 s^{-1}	0.0	[28]
(R97)	$N_2(a'\,^1\Sigma_u^-) \rightarrow N_2 + h\nu$ (177 nm)	1.0×10^2 s^{-1}	0.0	[29]
(R98)	$N_2(A\,^3\Sigma_u^+) \rightarrow N_2 + h\nu$ (293 nm)	0.5 s^{-1}	0.0	[29]
(R99)	$N_2(B\,^3\Pi_g) \rightarrow N_2(A\,^3\Sigma_u^+) + h\nu$ (1045 nm)	1.34×10^5 s^{-1}	0.0	[29]
(R100)	$N_2(C\,^3\Pi_u) \rightarrow N_2(B\,^3\Pi_g) + h\nu$ (336 nm)	2.45×10^7 s^{-1}	0.0	[29]
(R101)	$e + H_2O \rightarrow e + H_2O$	Cross section	0.0	[6]
(R102)	$e + H_2O \rightarrow 2e + H_2O^+$	Cross section	12.61	[6]
(R103)	$e + H_2O \rightarrow H + OH + e$	Cross section	7.0	[6]
(R104)	$e + H_2O \rightarrow H_2 + O(^1D) + e$	Cross section	7.4	[6]
(R105)	$e + H_2O \rightarrow H + OH(A) + e$	Cross section	9.15	[6]
(R106)[b]	$e + O \rightarrow e + O(^1D)$	$4.5 \times 10^{-15} \times \exp(-2.29/T_e)$ m^3 s^{-1}	0.0	[6]
(R107)[b]	$e + OH \rightarrow e + O + H$	$2.08 \times 10^{-13} \times T_e^{-0.76} \times \exp(-6.9/T_e)$ m^3 s^{-1}	0.0	[6]
(R108)	$OH^+ + H_2O \rightarrow H_3O^+ + O$	1.3×10^{-15} m^3 s^{-1}	0.0	[6]
(R109)	$H_2O^+ + H_2O \rightarrow H_3O^+ + OH$	1.85×10^{-15} m^3 s^{-1}	0.0	[6]
(R110)	$H_3O^+ + H_2O + M \rightarrow H_5O_2^+ + M$	$3.2 \times 10^{-39} \times (T_g/300)^{-4}$ m^6 s^{-1}	0.0	[6]
(R111)	$H_5O_2^+ + H_2O + M \rightarrow H_7O_3^+ + M$	$7.4 \times 10^{-39} \times (T_g/300)^{-7.5}$ m^6 s^{-1}	0.0	[6]
(R112)	$H_7O_3^+ + H_2O + M \rightarrow H_9O_4^+ + M$	$2.5 \times 10^{-39} \times (T_g/300)^{-8.1}$ m^6 s^{-1}	0.0	[6]
(R113)	$H_9O_4^+ + M \rightarrow H_7O_3^+ + H_2O + M$	$2.0 \times 10^{12} \times T_g^{-8.1} \times \exp(-8360/T_g)$ m^3 s^{-1}	0.0	[6]
(R114)	$He_m^* + H_2O \rightarrow He + H_2O^+ + e$	6.6×10^{-16} m^3 s^{-1}	0.0	[6]
(R115)	$He_m^* + H_2O \rightarrow He + OH^+ + H + e$	1.5×10^{-16} m^3 s^{-1}	0.0	[6]
(R116)	$He_m^* + H_2O_2 \rightarrow He + OH^+ + OH + e$	7.8×10^{-16} m^3 s^{-1}	0.0	[6]
(R117)	$He_2^* + H_2O \rightarrow H_2O^+ + 2He + e$	6.0×10^{-16} m^3 s^{-1}	0.0	[6]
(R118)	$He + O(^1D) \rightarrow O + He$	1.0×10^{-19} m^3 s^{-1}	0.0	[6]
(R119)	$2OH \rightarrow H_2O_2$	$1.5 \times 10^{-17} \times (T_g/300)^{-0.37}$ m^6 s^{-1}	0.0	[6]
(R120)	$OH(A) \rightarrow OH + h\nu$ (306.4 nm)	1.25×10^6 s^{-1}	0.0	[6]

[a] T_e is the electron temperature in kelvin.

[b] T_e is the electron temperature in eV;
T_g is the background temperature in kelvin.

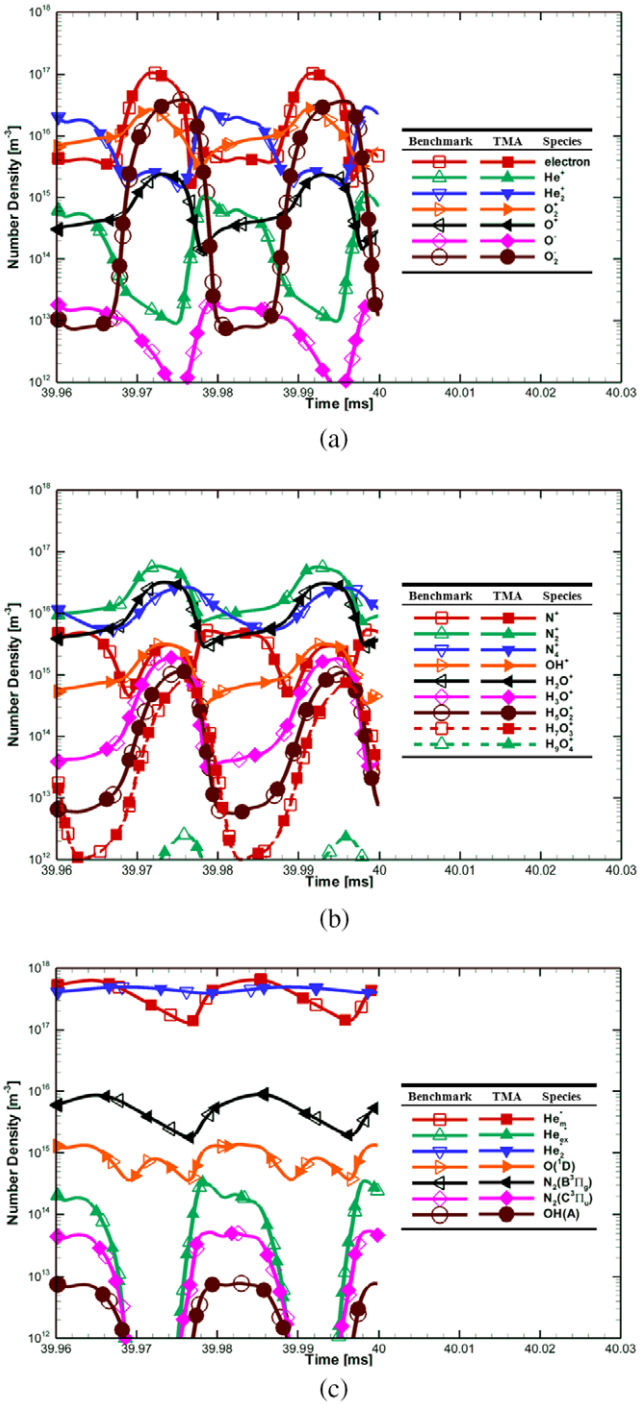

Figure 3. The comparison of temporal variations of the spatially averaged number densities of all the 'fast species', including the charged species (*a*), (*b*) and the 'fast' neutral species (*c*), in the last voltage cycle between the cases of benchmarking and TMA with the simulation conditions of 5 ICs, 5 SCs and 4 RSs.

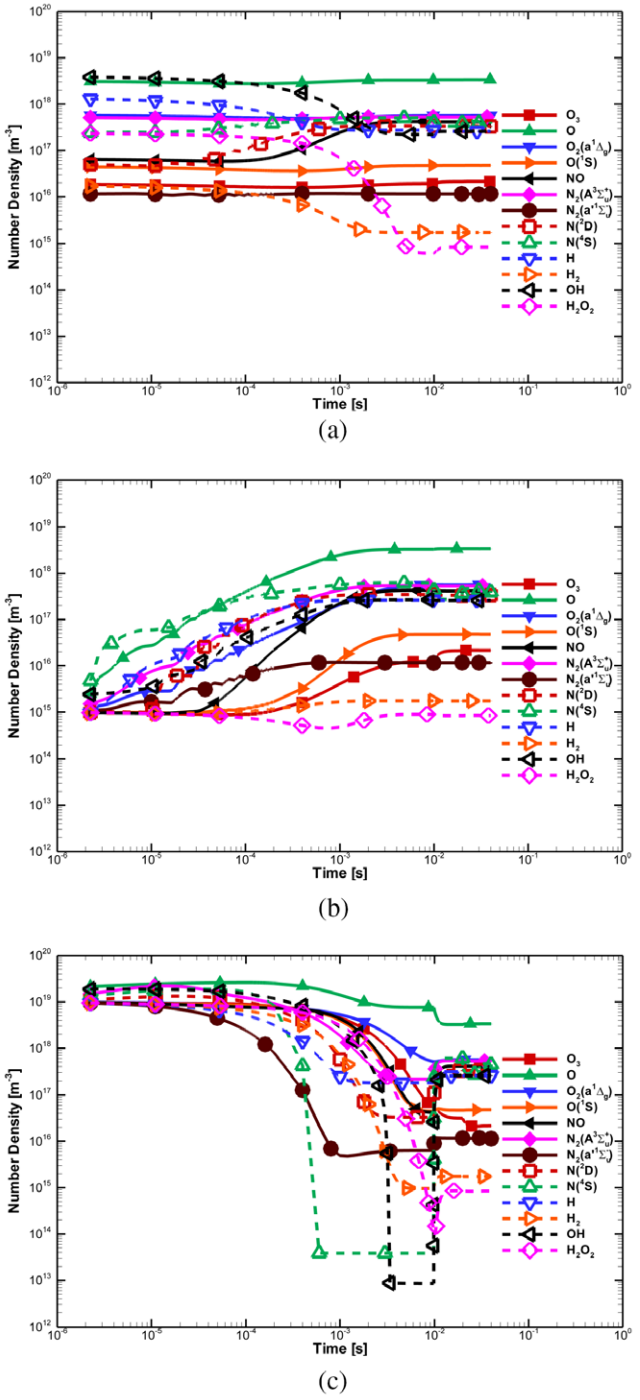

Figure 4. Temporal variation of number densities of various slow neutral species using TMA with the simulation conditions of 5 ICs, 5 SCs and 4 RSs. (*a*) Distributed initial densities, (*b*) low initial densities ($1.0 \times 10^{15}\,m^{-3}$) and (*c*) high initial densities ($1.0 \times 10^{19}\,m^{-3}$).

larger than that of nitric oxide and two orders larger than that of ozone, which is not uncommon, because the amount of molecular oxygen in the background gases is very small in the current study (only 10 ppm). The results are similar to those found in Murakami *et al* [23], in which the density of atomic oxygen is four orders larger than that of nitric oxide and one order larger than that of ozone. In their global modeling, background helium gas at atmospheric pressure conditions contains 0.5% O_2, an air impurity of 250 ppm and humidity of 50%. In our 1D modeling, the fraction of O_2 is much smaller than that of Murakami's conditions, which may lead to the current modeling results. Nevertheless, it is not necessary for the ozone concentration to be larger than the atomic oxygen concentration. The steady-state results of all

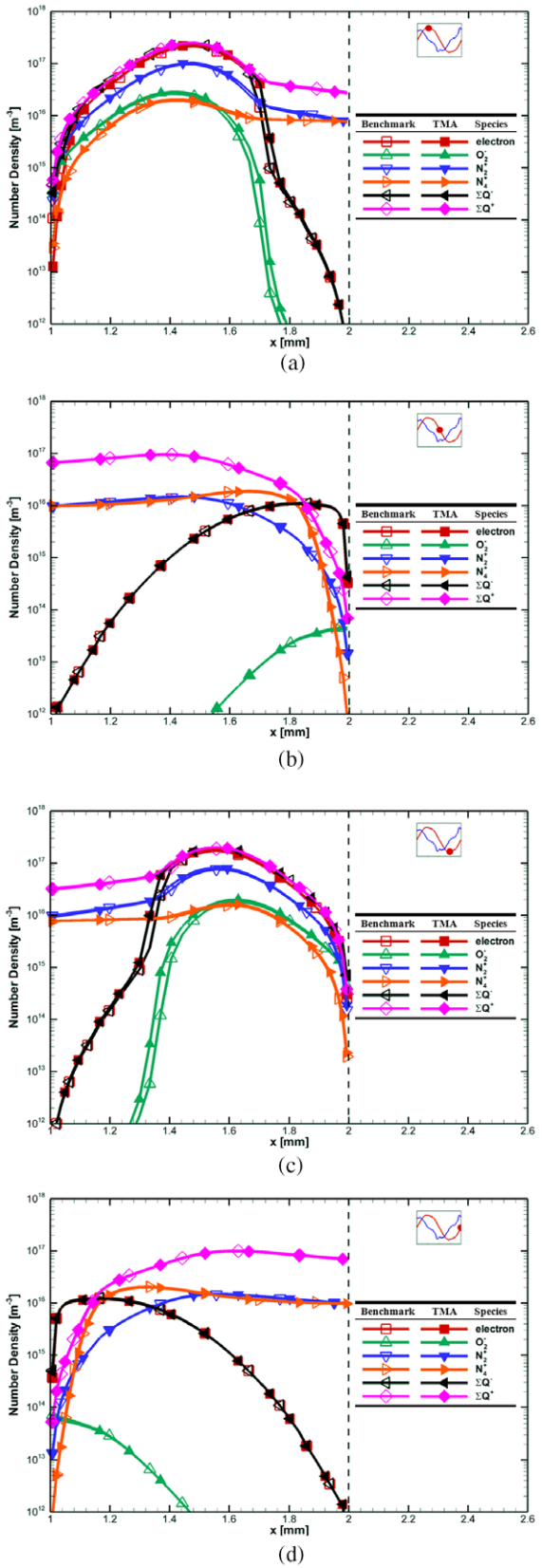

Figure 5. Comparison of the snapshots of the distributions of the number densities of the charged species between the benchmarking and TMA cases for some typical species in different phases of the last cycle before the simulation ends, where (*a*) $\varphi = 0.5\pi$, (*b*) $\varphi = \pi$, (*c*) $\varphi = 1.5\pi$ and (*d*) $\varphi = 2\pi$. Note all simulations were performed using TMA with the conditions of 5 ICs, 5 SCs and 4 RSs.

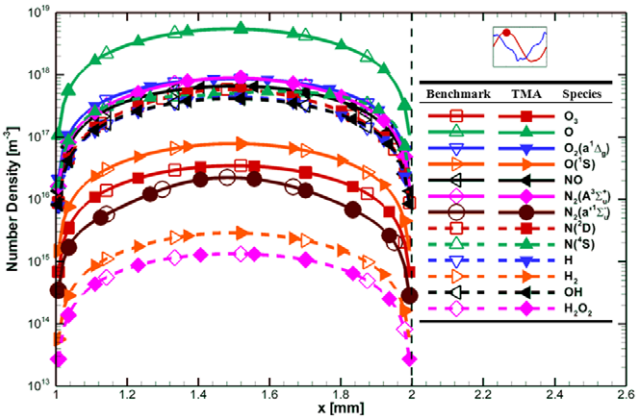

Figure 6. Comparison of the snapshots of the distributions of the number densities of the 'slow' neutral species between the benchmarking and TMA cases for some typical species at $\varphi = 0.5\pi$ of the last cycle before the simulation ends. Note all simulations were performed using TMA with the conditions of 5 ICs, 5 SCs and 4 RSs.

the 'slow' neutral species of the simulation using the TMA are nearly the same as those of the benchmarking case, although we have not shown the data of the latter in the same plot for the sake of clarity. In addition to the verification of the temporal variations of the spatially averaged number densities of all species using the TMA, we will verify the spatial distributions of the snapshots of the number densities of all species at different times within the last cycle to make sure the TMA can faithfully reproduce the data with the highest accuracy not only for spatially averaged temporal data, but also for instantaneous spatial data.

Figure 5 compares the snapshots of the distributions of the number densities of some charged species between the benchmarking and TMA cases in different phases of the last cycle of the simulation. In addition, the total number densities of the negative and positive charged species are presented in the plot for a better comparison. Again, the results clearly show that the TMA can faithfully reproduce the data of the benchmarking case. The slight discrepancy between them caused by the variation in simulation conditions of the TMA will be presented later in a systematic manner.

Figure 6 compares the snapshots of the distributions of the number densities of the 'slow' neutral species between the benchmarking and TMA cases at the end of the simulation of the last cycle. The reason we only present the snapshots at one instantaneous moment is that the data at different phases of the last cycle are essentially the same since they change very slowly for the 'slow' neutral species. Again, the comparison in figure 6 shows that the TMA data agree very well with the benchmarking data for all 'slow' neutral species.

Figure 7 illustrates the effect of the number of supplementary cycles on the relative difference of all the simulated spatially averaged number densities between the benchmarking and TMA, with the simulation conditions of five ICs and four RSs. The results show that, with only two SCs, the deviations of the simulated number densities using the TMA from those of the benchmarking are generally less than 10%, except for some species such as N^+ (23.75%),

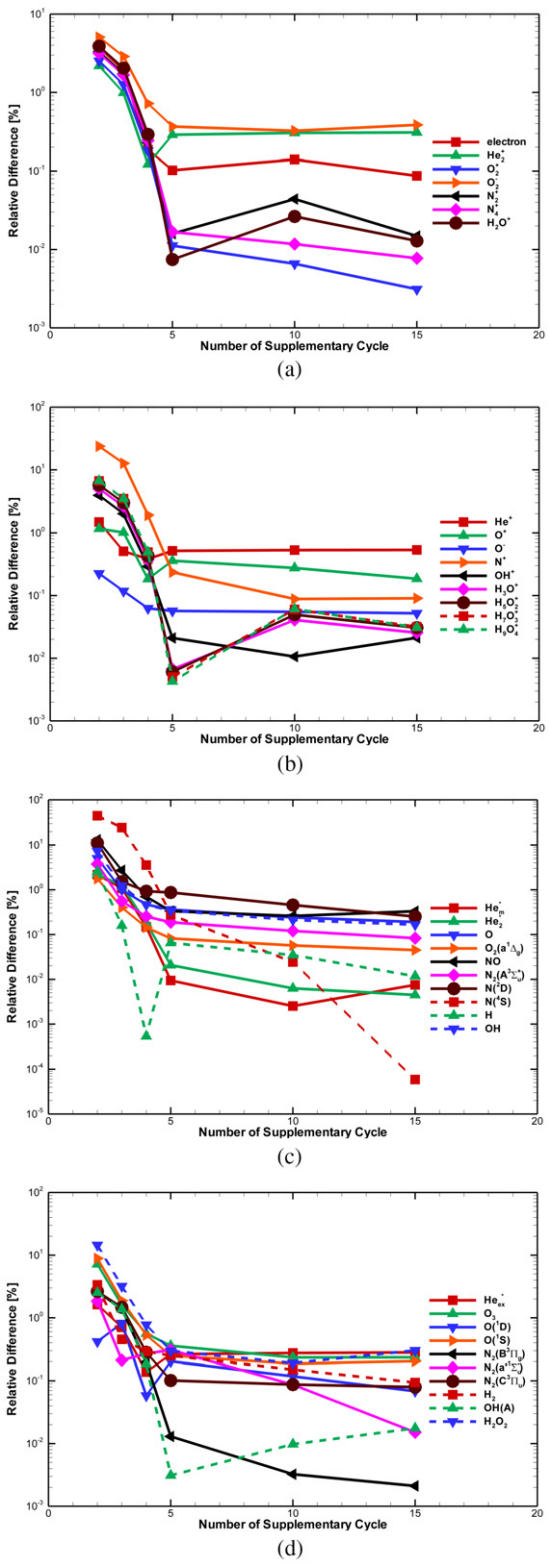

Figure 7. The effect of the number of supplementary cycles on the relative difference of simulated spatially averaged number densities between the benchmarking and TMA with the simulation conditions of 5 ICs and 4 RSs, where (*a*) the charged species whose cycle-averaged number densities are larger than $1.0 \times 10^{16}\,\mathrm{m}^{-3}$, (*b*) the charged species whose cycle-averaged number densities are less than $1.0 \times 10^{16}\,\mathrm{m}^{-3}$, (*c*) the neutral species whose cycle-averaged number densities are larger than $1.0 \times 10^{17}\,\mathrm{m}^{-3}$, (*d*) the neutral species whose cycle-averaged number densities are less than $1.0 \times 10^{17}\,\mathrm{m}^{-3}$.

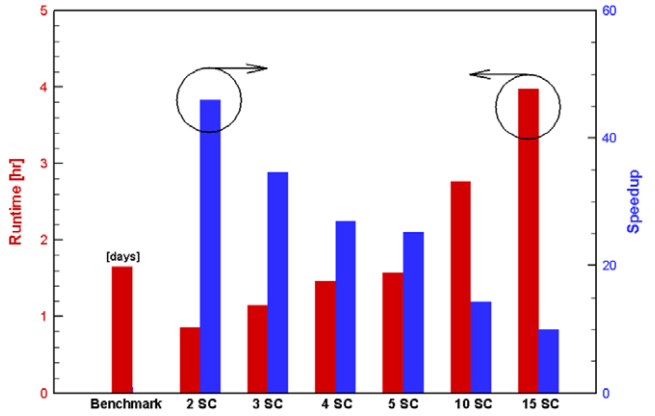

Figure 8. Comparison of computational time between the cases of benchmarking and TMA with the simulation conditions of 5 ICs, and 4 RSs considering different numbers of supplementary cycles.

NO (13.15%), N(^2D) (11.08%), N(^4S) (45.20%) and H_2O_2 (14.50%). The deviations of the simulated number densities using the TMA with four SCs from those of the benchmarking are generally less than 1%, except for some species such as N^+ (1.90%) and N(^4S) (3.57%). If we increase the number of SCs up to five, then the deviations become less than 1% for all the species. Since we have mentioned earlier that the selection of 'slow' and 'fast' neutral species is only 'qualitative', we would like to demonstrate that the improper classification of neutral species will lead to worse or even wrong convergence of the solution. Thus, we have tested a new case by treating, for example, He* (originally identified as a 'fast' neutral species) as a 'slow' neutral species under the same simulation conditions as those presented previously (five ICs, five SCs and four RSs) and the maximum deviation of the spatial-averaged density among different neutral species rises from 0.87% (N(^2D) for the original typical TMA case) to 3.33% (O^- for the new case). In addition, if we treat all neutral species as 'slow' neutral species, the spatial-averaged density of, for example, O(^1S) would become 2.7 times (270%) larger than the benchmarking case. However, one can imagine that the test matrix for varying all possibilities would be too large to be performed for systematic investigation in the current study, which may deserve future detailed investigation.

Figure 8 summarizes the comparison of the computational time between the TMA and benchmarking cases with the simulation conditions of five ICs and four RSs considering different numbers of supplementary cycles. The results demonstrate that a speed increase of about 46.0, 34.6, 27.0 and 25.3 times can be obtained, should the two, three, four and five SCs be used, respectively. For the former, using the TMA with five SCs, one can reduce the runtime from 40 h down to 94 min for the simulation of up to a physical time of 0.04 s. This demonstration gives us confidence in extending this TMA to a multi-dimensional fluid model, which we will describe briefly in the conclusion. In addition, if we relax the accuracy requirements for some species up to 44% for N(^4S) ($n = 4.0 \times 10^{17}\,\mathrm{m}^{-3}$) and 23% for N^+ ($n = 3.0 \times 10^{15}\,\mathrm{m}^{-3}$) while others deviate less than 10%, then our results with the conditions of two ICs, two RSs and two SCs show that the

runtime can be 92 times faster. Furthermore, if we further relax the accuracy requirements for some species up to 72% for $N(^4S)$ ($n = 4.0\times10^{17}\,m^{-3}$), 35% for N^+ ($n = 3.0\times10^{15}\,m^{-3}$), 31% for H_2O_2 ($n = 8.4\times10^{14}\,m^{-3}$) and 14% for O_3 ($n = 2.2\times10^{16}\,m^{-3}$), while others deviate less than 10%, then our results with the conditions of two ICs, one RS and two SCs show that the runtime can be 129 times faster.

4. Conclusion

In this study, we present and validate a temporal multi-scale algorithm (TMA) for the efficient fluid modeling of a one-dimensional gas discharge considering complex plasma chemistry. A helium atmospheric-pressure dielectric barrier discharge with impurities of oxygen, nitrogen and water vapor, comprising 36 species and 121 reaction channels, is used to demonstrate the effectiveness of the TMA in speeding up the simulation with essentially the same accuracy as the lengthy benchmarking fluid model using a single time-scale approach. The results show that the runtime can be dramatically reduced by 25.3 times and the deviations of simulated spatially averaged number densities are less than 1% for all species with the TMA simulation conditions of five initial cycles, four supplementary cycles and five repeated stages. In addition, a speed increase of ~90 times could be obtained, should the accuracy requirement decrease down to 44% for some species with the same simulation conditions, which is not unusual for this kind of simulation. Based on our experience, the size of the slow diffusion stage should be set approximately as the order of the largest characteristic diffusive time scale among the selected 'slow' neutral species.

For modeling most of the low- and atmospheric-pressure gas discharges, a multi-dimensional fluid model coupled with a gas flow solver is often required. Of course, a natural combination of the TMA with parallel computing is highly expected. Based on the success of the application of the TMA in one-dimensional fluid modeling in coupling the discharge and diffusion time scales, one can readily extend the idea by including the spatial distributions of background gas properties (e.g. the density, temperature and velocities) from the gas flow solver and feedback the proper cycle-averaged data from the fluid model to the gas flow solver as the source terms in different equations of conservations (mass, momentum and energy). This work is currently in progress and will be reported in the very near future.

Acknowledgments

The authors would like to express their sincere thanks for the computing resources provided by National Central University and National Center for High-Performance Computing of Taiwan through NSC 101-2221-E-009-041-MY3.

References

[1] Kim H C, Iza F, Yang S S, Radmilović-Radjenović M and Lee J K 2005 *J. Phys. D: Appl. Phys.* **38** R283
[2] Lee H W, Park G Y, Seo Y S, Im Y H, Shim S B and Lee H J 2011 *J. Phys. D: Appl. Phys.* **44** 053001
[3] Lin K-M, Hung C-T, Hwang F-N, Smith M R, Yang Y-W and Wu J-S 2012 *Comput. Phys. Commun.* **183** 1225–36
[4] Lin K-M, Hu M-H, Hung C-T, Wu J-S, Hwang F-N, Chen Y-S and Cheng G 2012 *Comput. Phys. Commun.* **183** 2550–60
[5] Gaens W V and Bogaerts A 2013 *J. Phys. D: Appl. Phys.* **46** 275201
[6] Liu D X, Bruggeman P, Iza F, Rong M Z and Kong M G 2010 *Plasma Sources Sci. Technol.* **19** 025018
[7] Kushner M J 2009 *J. Phys. D: Appl. Phys.* **42** 194013
[8] Sakiyama Y, Graves D B, Chang H-W, Shimizu T and Morfill G E 2012 *J. Phys. D: Appl. Phys.* **45** 425201
[9] Sakiyama Y and Graves D B 2013 *Plasma Sources Sci. Technol.* **22** 012003
[10] Chiang M-H, Liao K-C, Lin I-M, Lu C-C, Huang H-Y, Kuo C-L, Wu J-S, Hsu C-C and Chen S-H 2010 *Plasma Chem. Plasma Process.* **30** 553–63
[11] Hagelaar G J M and Pitchford L C 2005 *Plasma Sources Sci. Technol.* **14** 722
[12] Yuan X and Raja L L 2003 *IEEE Trans. Plasma Sci.* **31** 495–503
[13] Mangolini L, Anderson C, Heberlein J and Kortshagen U 2004 *J. Phys. D: Appl. Phys.* **37** 1021
[14] Waskoenig J, Niemi K, Knake N, Graham L M, Reuter S, Gathen V S der and Gans T 2010 *Plasma Sources Sci. Technol.* **19** 045018
[15] Ellis H W, Pai R Y, McDaniel E W, Mason E A and Viehland L A 1976 *At. Data Nucl. Data Tables* **17** 177–210
[16] Viehland L A and Mason E A 1995 *At. Data Nucl. Data Tables* **60** 37–95
[17] Ellis H W, McDaniel E W, Albritton D L, Viehland L A, Lin S L and Mason E A 1978 *At. Data Nucl. Data Tables* **22** 179–217
[18] Ivanov A V, Trakhtenberg S, Bertram A K, Gershenzon Y M and Molina M J 2007 *J. Phys. Chem.* A **111** 1632–7
[19] Bird R B, Stewart W E and Lightfoot E N 2007 *Transport Phenomena* (New York: Wiley)
[20] Poling B E, Prausnitz J M and O'Connell J P 2001 *The Properties of Gases and Liquids* (New York: McGraw-Hill)
[21] Petrović D, Martens T, van Dijk J, Brok W J M and Bogaerts A 2009 *J. Phys. D: Appl. Phys.* **42** 205206
[22] Hung C-T, Chiu Y-M, Hwang F-N, Chiang M-H, Wu J-S and Wang Y-C 2011 *Plasma Chem. Plasma Process.* **31** 1–21
[23] Murakami T, Niemi K, Gans T, O'Connell D and Graham W G 2013 *Plasma Sources Sci. Technol.* **22** 015003
[24] Martens T, Bogaerts A, Brok W and van Dijk J 2007 *Anal. Bioanal. Chem.* **388** 1583–94
[25] Lee D, Park J M, Hong S H and Kim Y 2005 *IEEE Trans. Plasma Sci.* **33** 949–57
[26] Tochikubo F, Uchida S, Yasui H and Sato K 2009 *Japan. J. Appl. Phys.* **48** 076507
[27] Martens T, Bogaerts A, Brok W J M and van Dijk J 2008 *Appl. Phys. Lett.* **92** 041504
[28] Kossyi I A, Kostinsky A Y, Matveyev A A and Silakov V P 1992 *Plasma Sources Sci. Technol.* **1** 207
[29] Capitelli M 2000 *Plasma Kinetics in Atmospheric Gases* (Berlin: Springer)